Int J Fract (2014) 190:99–110
DOI 10.1007/s10704-014-9977-x

ORIGINAL PAPER

Stretchability of indium tin oxide (ITO) serpentine thin films supported by Kapton substrates

Shixuan Yang · Becky Su · Ghassan Bitar · Nanshu Lu

Received: 23 July 2014 / Accepted: 21 October 2014 / Published online: 7 November 2014

Abstract Indium tin oxide (ITO) has been widely used as the electrode material in touch-screen displays and solar cells attributing to its combined high electrical conductivity and optical transparency. Moving forward from wafer based electronics to flexible/stretchable electronics, brittle electronic materials like ITO are significantly hindering the deformability of the integrated systems. To minimize strains in inorganic materials when subjected to stretch, thin metallic and ceramic films can be patterned into serpentine shapes. Although metallic serpentines have received extensive studies, experimental investigations on ceramic serpentines have not been reported. We perform uniaxial tension tests on Kapton-supported ITO serpentine thin films with in situ electrical resistance measurements. It is found that the narrower serpentine ribbons are more stretchable than their wider counterparts. We propose a generic empirical equation to predict the stretchability using three dimensionless geometric parameters. Conclusions reached for Kapton-supported ITO serpentine films are generally applicable to gold, silicon, and other stiff serpentine films bonded to stiff polymer substrates such as Kapton and polyethylene terephthalate.

S. Yang · B. Su · G. Bitar · N. Lu (✉)
Center for Mechanics of Solids, Structures and Materials, Department of Aerospace Engineering and Engineering Mechanics, Center for Nanomanufacturing Systems for Mobile Computing and Mobile Energy Technologies (NASCENT), Texas Materials Institute, University of Texas at Austin, Austin, TX 78712, USA
e-mail: nanshulu@utexas.edu

Keywords Indium tin oxide · Serpentine · Kapton · Stretchability · Resistance

1 Introduction

A booming direction for integrated circuit technology is flexible and stretchable electronics. Typical applications of flexible electronics include but are not limited to paper-like electronic displays (Rogers et al. 2001), rollable solar cells (Yoon et al. 2008), human-mimetic robotic skins (Sekitani and Someya 2012) and bio-integrated electronics (Kim et al. 2012). Conventional semiconductors such as silicon and gallium arsenide, conductive materials such as metals and indium tin oxide (ITO), and dielectric materials such as silicon oxides and silicon nitrides, are intrinsically stiff and even brittle, and are therefore hard to deform. However, they are still attractive functional materials to be used in flexible electronics attributing to their superior electronic performance in terms of mobility, on-off ratio, conductivity, dielectric constant, as well as their excellent chemical stability in contrast to organic electronic materials (Service 2006). Therefore, to enhance the deformability of inorganic electronic materials, several mechanics strategies have been developed. For example, semiconducting nanoribbons of silicon and gallium arsenide can be integrated on elastomer substrates with sinusoidal periodic wrinkles or buckles (Khang et al. 2006; Sun et al. 2006). When the elastomer substrates are stretched, the buckled ribbons are able to accommo-

date large applied tensile or compressive displacements through rigid body rotation, leaving small strains in the ribbons. Another stretchable structure comprises of isolated stiff device islands interconnected by serpentine-shaped thin metal films. Due to the large elastic mismatch between the islands and the elastomer substrate, the compliant serpentines will have to extend much more than the rigid islands, leaving the brittle electronic materials on the rigid islands intact (Kim et al. 2008, 2011a, c; Xu et al. 2013). Moreover, with the development of bio-integrated electronics, it emerges that not only the stretchability, but also the structure compliance are critical for the mechanical compatibility between electronics and bio-tissues. A recent study on epidermal electronics has shown that a filamentary serpentine network, where all the rigid islands at the intersections of the network are eliminated, can be much softer compared to an island-plus-serpentine network (Kim et al. 2011b; Widlund et al. 2014). This finding has enabled the mechanically invisible electronic tattoos to be intimately integrated with human skin for electrophysiological, thermal, and hydration sensing (Huang et al. 2012; Kim et al. 2011b; Webb et al. 2013; Yeo et al. 2013). In addition to metallic filamentary serpentines, silicon nanomembranes as a brittle material have also been patterned into filamentary serpentines to achieve epidermal amplifiers and solar cells (Kim et al. 2011b).

The mechanics of metallic serpentines has been studied extensively through both experimental (Gray et al. 2004; Hsu et al. 2009, 2011; Kim et al. 2008) and theoretical means (Li et al. 2005; Zhang et al. 2013a, b, 2014; Widlund et al. 2014). However, so far, there is no experimental investigation or unified theory available to reveal the stretchability of brittle serpentine films of various shapes, on any type of polymer substrates. We here define *stretchability* as the critical tensile strain applied to the substrate at which crack starts to appear in the thin film. This paper is limited to uniaxial tension because convex bending also leads to tensile strains on the top surface of the polymer substrate where serpentines reside. The stretchability of brittle serpentine films on polymer substrates can be determined by observing the crack density evolution as a function of the applied strain. The point where crack density starts to deviate from zero can be identified as the *strain-to-rupture*, i.e. stretchability. However, counting crack density at different amount of applied strains could be tedious. Fortunately, it has been experimentally proved that the electrical resistance is closely correlated with the crack density within electrically conductive thin films. Therefore resistance versus applied strain curves have been widely adopted to indicate the stretchability of thin metal (Lu et al. 2010, 2007; Niu et al. 2007) and ITO films (Peng et al. 2011, 2012).

Thin ITO films have been a popular electrode material in flat panel displays (Betz et al. 2006) and solar cells (Schmidt et al. 2009) attributing to their combined high electrical conductivity and optical transparency. However, ITO is not mechanically favorable in flexible/stretchable electronics due to its brittle nature (Zheng et al. 2012). Cracks are observed at applied tensile strains around 1 % in polymer-supported blanket thin ITO films (Leterrier et al. 2004; Peng et al. 2011, 2012). Enhancing the stretchability of thin ITO films bonded on polymer substrates is practically significant for the development of flexible and rollable displays and solar cells.

In this paper, stretchability of Kapton-supported serpentine ITO thin film is experimentally measured and numerically simulated. Serpentine shapes are varied systematically and the effects of serpentine ribbon width, arc radius, arc angle and arm length are carefully revealed. An empirical relation between serpentine geometry and stretchability is proposed and validated. The paper is organized as follows. Section 2 describes the experimental procedures and results. Finite element modeling (FEM) and analytical analysis are provided in Sects. 3 and 4, respectively. Conclusions are offered in Sect. 5.

2 Experimental

Specimens for tension tests are fabricated as follows. Polyimide foils (Dupont Kapton 50NH, 12.7 μm) are first cleaned in Acetone and then isopropyl alcohol (IPA) in an ultrasonic cleaner followed by DI water rinse. After dehydration, the Kapton substrate is covered by a molybdenum stainless steel stencil (Towne Technologies, Inc.) with straight and serpentine-shaped openings and is then loaded into a sputter deposition chamber (AJA International, Inc.). When the base pressure reaches 5×10^{-6} torr, the Kapton substrate is first cleaned by argon (Ar) plasma with radio frequency (RF) power. Immediately after the RF cleaning, 200 nm thick ITO is sputtered from an ITO target (Kurt J. Lesker) onto the Kapton substrate through the openings on the stencil with a working gas pressure of 2

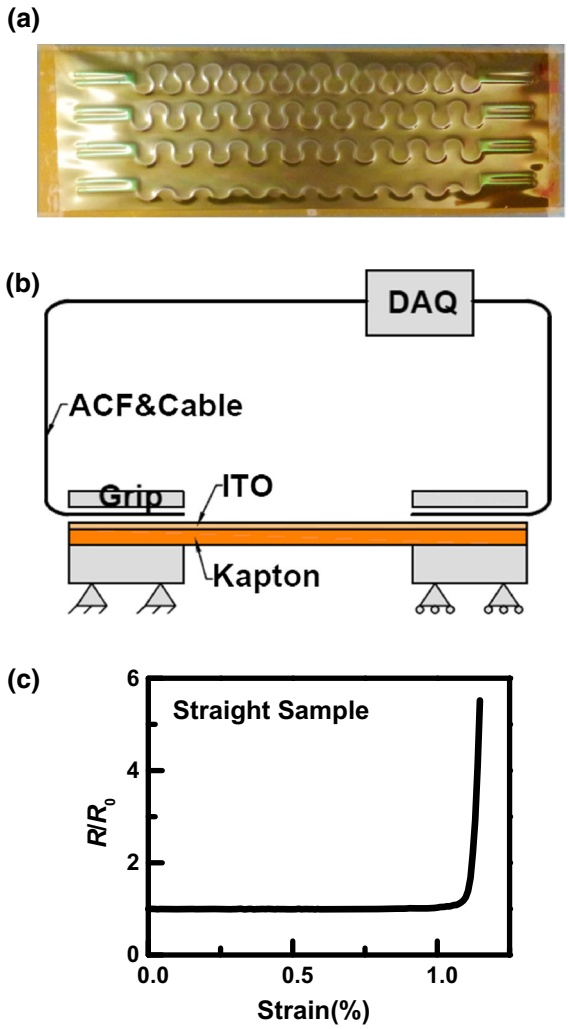

Fig. 1 Experimental setup. **a** *Top view* of a group of four ITO serpentine thin films sputtered on a 12.7 μm thick Kapton substrate. **b** Schematics of the experimental setup for the in situ electrical resistance measurement of the ITO serpentines subjected to uniaxial tension. **c** A resistance versus applied strain curve of a linear ITO ribbon on Kapton substrate

mtorr and a RF power of 65 W. After taking the ITO coated Kapton out of the sputter chamber, the straight specimens are cut into long rectangular strips and the serpentine specimens are cut into rectangular pieces each including a group of four or five serpentine ribbons with systematically varied shapes, as shown in Fig. 1a.

To perform uniaxial tension test, Kapton sheets with ITO coatings are gripped on a home-made manual stretcher and applied displacements are obtained by measuring the changes of the gauge length between the grips. The applied strain, ε_{app}, is hence calculated as the ratio of the applied displacement to the initial gauge length. A schematic of the experimental set up with in situ electrical resistance measurement is shown in Fig. 1b. The ITO ribbons are connected through an anisotropic conductive film (ACF) to a multi-channel data acquisition (DAQ) system (NI USB-6225) which is configured to conduct simultaneous resistance measurements up to five channels. The normalized resistance versus applied strain curve for a straight ITO specimen is provided in Fig. 1c. Due to the instantaneous channel crack propagation in a brittle material like ITO, upon crack initiation, it will not be too long before the ITO ribbon completely loses electrical conductivity, where the resistance approaches infinite. If we adopt a failure criterion of 10 % deviation from initial resistance, the strain-to-rupture of this straight ITO-on-Kapton specimen is found to be 1.08 %, which is in good agreement with previous strain-to-rupture results of straight ITO-on-Kapton specimens (∼1 %) (Peng et al. 2011), indicating that our electrical resistance measurement can be a good indicator of the cracking status in straight ITO ribbons.

Figure 2 summarizes different shapes of serpentines we have tested. A serpentine shape can be analytically described by four independent geometric parameters as labeled in Fig. 2a (Widlund et al. 2014): the ribbon width w, the arc radius r, the arc angle α, and the arm length l. As a result, three dimensionless parameters are adopted in this study: the normalized ribbon width w/r, the normalized arm length l/r, and the arc angle α. The larger arc angle will represent a more tortuous serpentine shape. By tuning the three dimensionless parameters, different serpentine shapes can be obtained. Some examples are shown in Fig. 2b. Group (a) reveals the effect of w/r with fixed α and l/r whereas Group (b) focuses on the effect of l/r with fixed α and w/r. Groups (c) and (d) both highlight the effect of α but at different w/r and l/r, respectively. We can also refer to Group (a) as basic serpentine, Group (b) as U-shaped serpentine, Group (c) as horseshoe-shaped serpentine, and Group (d) as V-shaped serpentine.

To validate that resistance measurement can also sufficiently reflect the cracking status in serpentine thin films, we try to compare the strains-to-rupture measured by crack density and electrical resistance. Semi-in situ scanning electron microscope (SEM) tension test is preformed to obtain the crack density versus

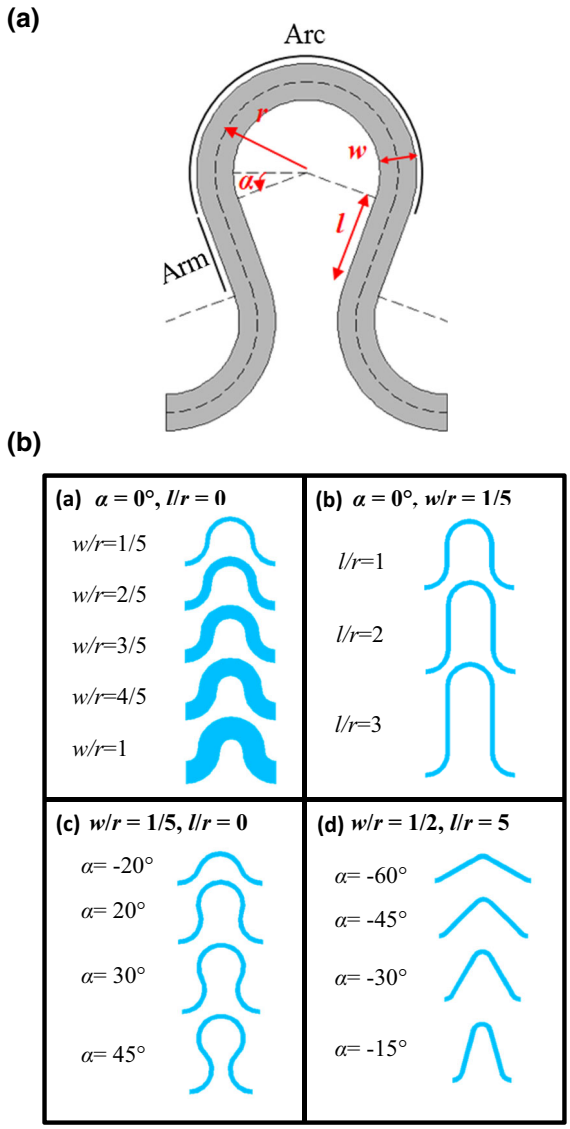

Fig. 2 Systematically varied serpentine shapes. **a** Geometrical parameters that are used to define the shape of a serpentine, where w, r, l, and α represent the ribbon width, the arc radius, the arm length, and the arc angle respectively. **b** A table of different groups of serpentines to study the effect of w/r in Group (*a*) (regular serpentines), l/r in Group (*b*) (U-shaped serpentines), α in Group (*c*) (horseshoe-shaped serpentines) and Group (*d*) (V-shaped serpentines)

applied strain curve and the results are summarized in Fig. 3. The SEM picture in Fig. 3a indicates that when the Kapton-bonded serpentine ribbons are subjected to uniaxial stretch, the inner edge of the crest of the serpentine is where cracks would like to initiate. This observation can later be explained by the strain concentration at the inner crest using FEM. For brittle ceramic materials, most channel cracks initiated at the inner crest of the arc will propagate throughout the width of the serpentine ribbon and hence completely cut off the electrical current. We therefore focus on this area and obtain a series of snapshots at different amount of applied strains as shown in Fig. 3b. The defect particle appearing in all snapshots serves as a reference point to align the frames. Starting with a crack free snapshot at $\varepsilon_{app} = 1.3\,\%$, a channel crack perpendicular to the tensile (horizontal) direction first emanates from the defect particle at $\varepsilon_{app} = 1.4\,\%$. Since then, the number of cracks within the rectangular box has gradually increased with increasing ε_{app}. If we define *crack density* as the number of cracks per millimeter along the horizontal direction, a crack density versus applied strain curve (black) can be offered in Fig. 3c, along with the resistance versus applied strain curve (blue) which is obtained from the semi-in situ electrical measurement. By plotting the two curves with shared horizontal axis, it is easy to compare the strains at which they start to blow up, i.e. the strains-to-rupture. By adopting the "10 % deviation" criterion, the strain-to-rupture deduced from the crack density measurements is 1.3 % whereas it is determined to be 1.45 % from the resistance measurement. Similar discrepancy between crack density and electrical resistance measurements has been observed in straight ITO-on-Kapton specimens (Peng et al. 2011). Figure 3d offers a possible explanation to such discrepancy. Defects in ITO thin films induced either by imperfections in the Kapton substrates or during ITO deposition tend to give rise to half or misaligned channel cracks, as highlighted in Fig. 3d. The presence of these types of cracks has less effect on the overall resistance of the ribbon compared to perfectly straight channel cracks shooting across the whole ribbon width. Therefore there is a small lag of strain to blow up in the resistance curve compared to the crack density curve. Despite of the small lag, the resistance is able to capture the failure of the ITO serpentine in a much more experimentally economic way. Hence we will determine the strain-to-rupture of the ITO serpentines only by electrical resistance measurements.

Resistance results of different ITO serpentine shapes as a function of the applied strain are plotted in Fig. 4. Curves within each figure come from serpentine ribbons on the same piece of Kapton substrate and are measured simultaneously via the multi-channel DAQ.

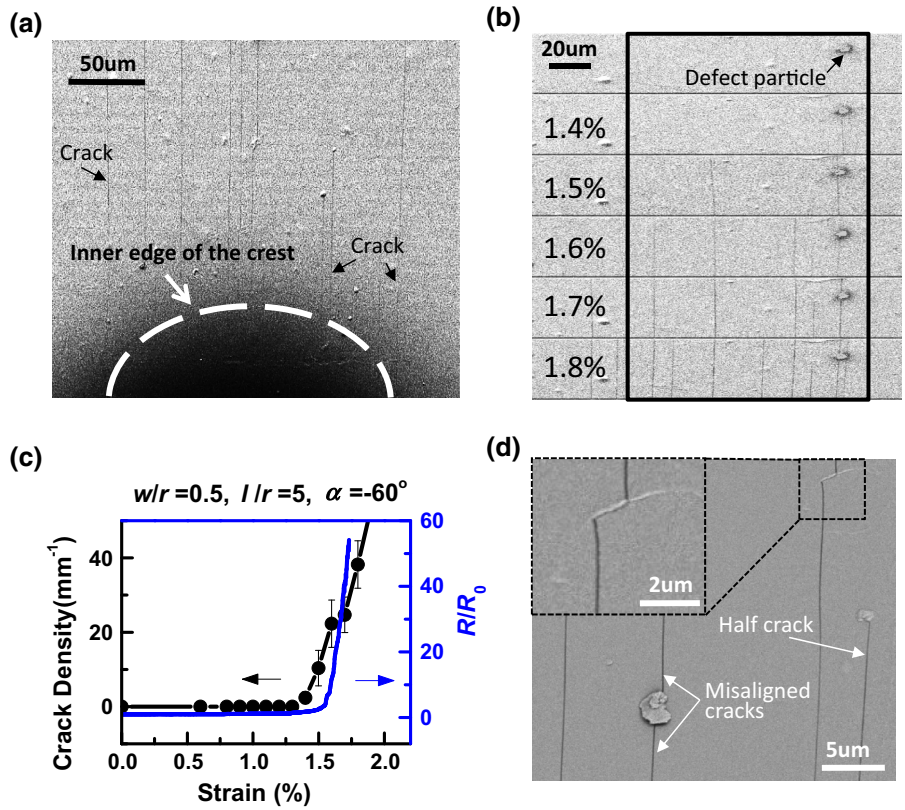

Fig. 3 Channel cracks in ITO. **a** One of many SEM micrographs showing channel cracks emanating from the inner edge of the crest and propagating perpendicular to the tensile (horizontal) direction. **b** A sequence of SEM snapshots showing the evolution of crack density with increased applied strain. **c** The crack density and electrical resistance of an ITO serpentine as functions of the applied strain. Strains at which the curves blow up are defined as the strain-to-rupture. **d** Half or misaligned cracks are associated with localized defects in ITO films

Each serpentine shape has been tested at least three times but only one representative curve is shown in Fig. 4. Figure 4a studies the effect of w/r with l/r fixed to be 0 and α fixed to be 0°, which corresponds to the basic serpentines as illustrated in Group (a) of Fig. 2b. It is evident from Fig. 4a that the effect of w/r is monotonic, i.e. as w/r decreases, the strain-to-rupture always increases. This indicates that the narrower serpentine ribbons are more stretchable, provided the same arm length and arc angle. Among the four serpentine shapes we have tested, the one with $w/r = 0.2$ exhibit a strain-to-rupture of 1.25 %, which is 15.7 % higher compared to the straight ribbons as shown in Fig. 1c. Despite of the enhancement, the stretchability of ITO serpentine ribbons bonded to Kapton substrate is still far less than freestanding or elastomer-supported metallic serpentine ribbons (Gray et al. 2004; Hsu et al. 2009; Kim et al. 2008; Li et al. 2005) due to first the constraint from the stiff Kapton substrate which suppresses both in-plane rigid body rotation and out-of-plane twist of the ribbons and second the intrinsic brittleness of the ITO. It has been verified by both side views of the stretched specimens and FEM that the out-of-plane deformation is negligible. Figure 4b studies the effect of l/r with w/r fixed to be 0.2 and α fixed to be 0°, corresponding to the U-shaped serpentines as illustrated in Group (b) of Fig. 2b. Surprisingly, the stretchability seems to be almost independent of the arm length. Similar conclusions have been reached for the effect of α, as shown in Fig. 4c, where w/r is fixed to be 0.2 and l/r is fixed to be 0, which corresponds to the U-shaped serpentines as illustrated in Group (c) of Fig. 2b. Figure 4d studies the effect of α for V-shaped serpentines, with w/r fixed to be 0.5, l/r fixed to be 0 and α varying from $-60°$ to $-15°$, corresponding to the V-shaped serpentines as illustrated in Group (d) of Fig. 2b. Although serpentines with $\alpha = -45°$, $-30°$, and $-15°$ share very similar stretchability, $\alpha = -60°$ serpentine which is the top one of Group (d) in Fig. 2b clearly shows lower stretchability. All above experimental observations can be explained by FEM results in Sect. 3 and an empirical equation in Sect. 4.

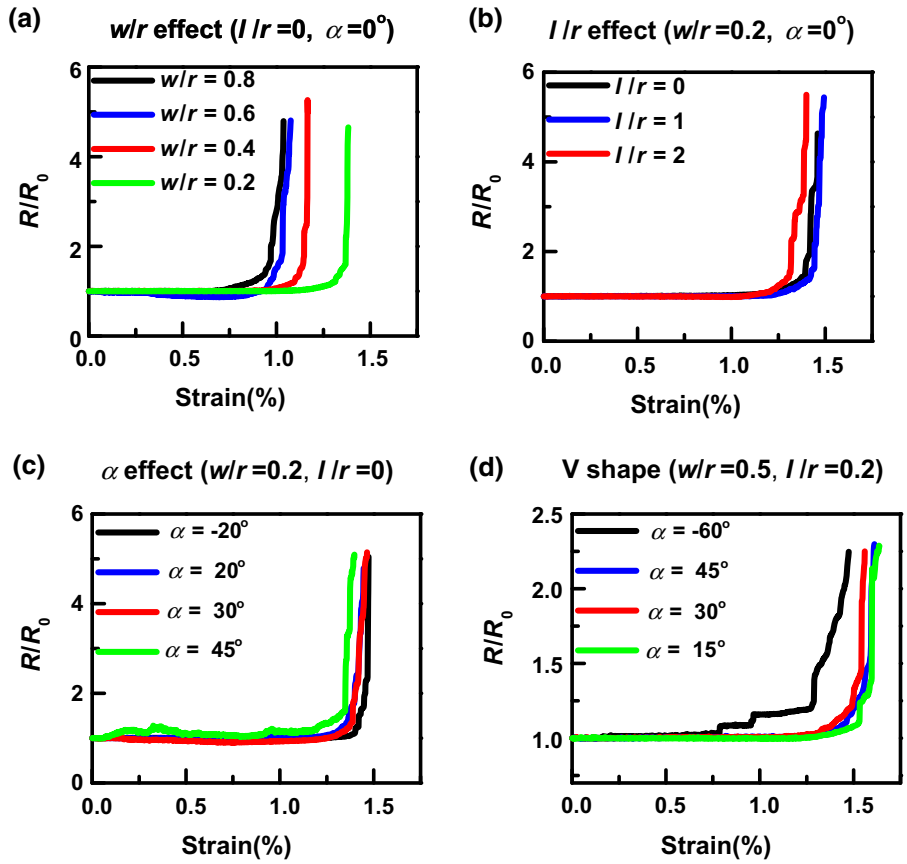

Fig. 4 Results of the multi-channel electrical resistance measurement during tension tests. **a** Effect of w/r: smaller w/r leads to delayed resistance blow-up. **b** Effect of l/r is negligible on the failure strain. **c** Effect of α on the stretchability of horseshoe-shaped serpentines is also negligible. **d** Effect of α on V-shaped serpentines is only significant when α falls in the far negative (less tortuous serpentines)

3 Finite element simulations

ABAQUS/CAE is used to build the FEM of a unit cell of the Kapton-supported ITO serpentine as depicted in Fig. 5a and the jobs are run on Texas Advanced Computing Center's (TACC) Dell Linux cluster. Due to the large difference in ITO and Kapton thicknesses (200 nm vs. 12.7 μm), the ITO thin film is modeled by shell element, whereas the Kapton substrate is modeled by 3D solid element. ITO and Kapton are assumed to be linear isotropic materials with moduli 118 and 2.5 GPa, and Poisson's ratios 0.27 and 0.34, respectively. Tie constraint is applied between the substrate and the film to ensure perfect bonding. Tensile strain $\varepsilon_{app} = 1\,\%$ is applied on the Kapton substrate along the x direction. Nonlinear analysis (nlgeom) is adopted in ABAQUS simulations for better accuracy.

Simulations for all serpentine groups shown in Fig. 2b are performed and the results are given in Fig. 5b–f. Figure 5b offers a representative contour plot of the normal strain in x-direction (ε_{xx}) of an ITO serpentine with shape $w/r = 0.2$, $l/r = 0$, and $\alpha = 0°$. It is obvious from the strain distribution that the strain concentration always occurs at the inner edge of the crest of the arc, which is consistent with our experimental observation of preferred crack initiation sites (Fig. 3a). Similar conclusion has also been drawn from our previous analysis and experiments on freestanding serpentines under plane strain condition (Widlund et al. 2014). Elastomer-supported serpentine ribbons, however, sometimes tend to rupture at the crest-to-arm transition zone mostly due to out-of-plane twist (Hsu et al. 2009).

For brittle materials like ITO, if we adopt the failure criterion of $\varepsilon_{max} = \varepsilon_{cr}$ where $\varepsilon_{cr} = 1.08\,\%$ is the intrinsic strain-to-rupture obtained by measuring straight ITO-on-Kapton specimens as shown Fig. 1c and ε_{max} is obtained by FEM under ε_{app}, the following equation should hold

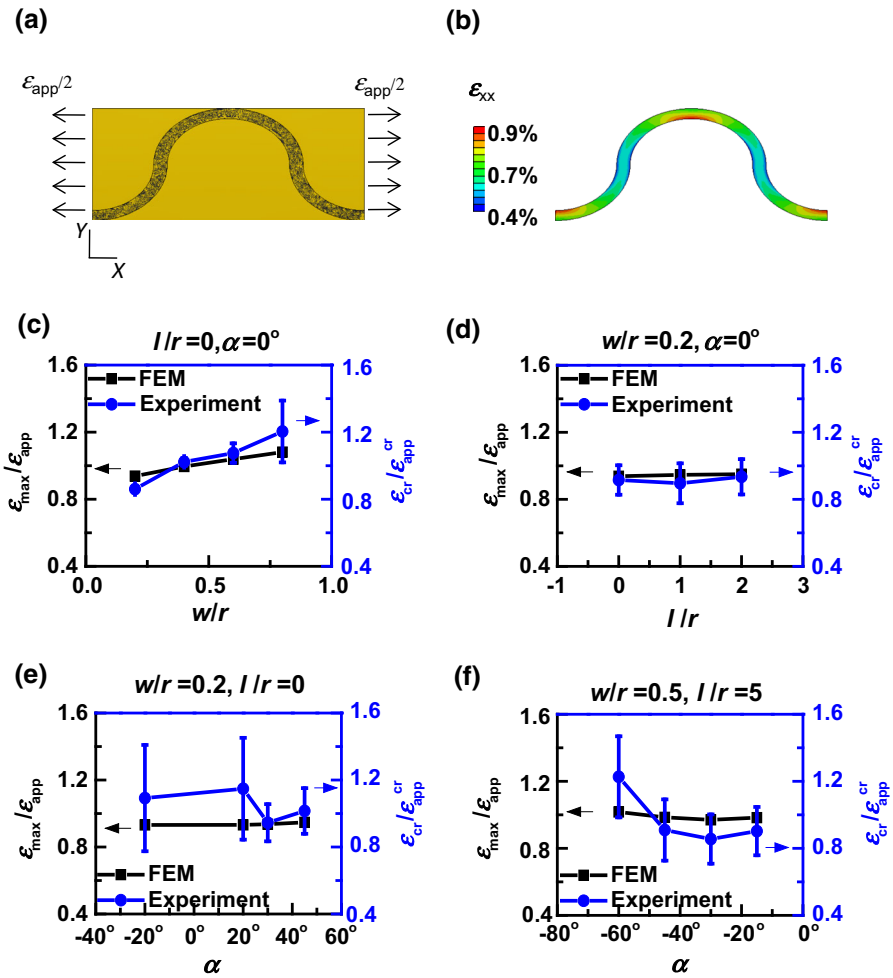

Fig. 5 Comparison between FEM and experimental results. **a** Boundary condition and **b** contour plot of ε_{xx} of a unit cell serpentine under applied strain $\varepsilon_{app} = 1\,\%$ on the Kapton substrate. **c** Effect of w/r: narrower ribbons render lower strains. Effects of **d** l/r on U-shaped and **e** α on horseshoe-shaped serpentines are negligible. **f** Effect of α on V-shaped serpentines is not monotonic

$$\frac{\varepsilon_{max}}{\varepsilon_{app}} = \frac{\varepsilon_{cr}}{\varepsilon_{app}^{cr}} \tag{1}$$

where ε_{app}^{cr} denotes the stretchability of Kapton-bonded serpentine beyond which the ribbon is considered fully ruptured and hence no longer electrically conductive. Therefore ε_{app}^{cr} can be experimentally determined from the resistance versus applied strain curve. Based on Eq. (1), we can also predict ε_{app}^{cr} by using FEM results of $\varepsilon_{max}/\varepsilon_{app}$:

$$\varepsilon_{app}^{cr} = \frac{\varepsilon_{cr}}{\varepsilon_{max}/\varepsilon_{app}} \tag{2}$$

which shows an inverse relation between stretchability and $\varepsilon_{max}/\varepsilon_{app}$. When $\varepsilon_{max}/\varepsilon_{app} < 1$, the serpentine shape can help enhance the stretchability beyond that of a straight ribbon. When $\varepsilon_{max}/\varepsilon_{app} > 1$, the serpentine actually has an effect of degrading the stretchability. A quantitative comparison between FEM and experimental results is offered in Fig. 5c–f. Black curves are plotting the left hand side of Eq. (1) with FEM results and the blue curves are plotting the right hand side of Eq. (1) with experimental results. Therefore in the most ideal cases, black and blue curves should fully overlap. Figure 5c studies the effect of w/r. The monotonic increase of $\varepsilon_{max}/\varepsilon_{app}$ with increased w/r in both experimental and FEM curves indicates reduced stretchability in wider ribbons. For serpentine ribbons with $w/r > 0.4$, their stretchability are going to be lower than straight ribbons. Figure 5d, e confirm by both FEM and experimental results that the effects of l/r and α are negligible when w/r is small ($w/r = 0.2$

for both cases). Figure 5f focuses on the effect of α for V-shaped serpentines. The effect is more significant when α approaches the far negative.

$$\frac{b}{s}=\begin{cases}\dfrac{\sqrt{\frac{2w}{r}}}{2\cos(\alpha)-\frac{l}{r}\sin(\alpha)} & \alpha\geq\alpha_0\\ \dfrac{\left(\frac{w}{r}+2\right)\sec(\alpha)-\left(\frac{w}{r}-2\right)\tan(\alpha)}{4\cos(\alpha)-\frac{2l}{r}\sin(\alpha)} & \alpha<\alpha_0 \text{ and } l\geq l_0\\ 1+\dfrac{\sqrt{k}}{-2\cos(\alpha)+\frac{l}{r}\sin(\alpha)} & \alpha<\alpha_0 \text{ and } l_1\leq l<l_0\\ 1 & \alpha<\alpha_0 \text{ and } l<l_1\end{cases} \tag{3}$$

$$\frac{b}{r}=\begin{cases}2\sqrt{\frac{2w}{r}} & \alpha\geq\alpha_0\\ \left(\frac{w}{r}+2\right)\sec(\alpha)-\left(\frac{w}{r}-2\right)\tan(\alpha) & \alpha<\alpha_0 \text{ and } l\geq l_0\\ -2\left(-2\cos(\alpha)+\frac{l}{r}\sin(\alpha)+\sqrt{k}\right) & \alpha<\alpha_0 \text{ and } l_1\leq l<l_0\\ 4\cos(\alpha)-\frac{2l}{r}\sin(\alpha) & \alpha<\alpha_0 \text{ and } l<l_1\end{cases} \tag{4}$$

4 Empirical geometry–stretchability relation

To predict the stretchability of Kapton-supported serpentine thin films, a formulation is desirable. An empirical equation is fitted using three new dimensionless geometric variables b/s, b/r and w/h, where b is the breadth of a unit cell, and s and $h$are the total length and height of one unit cell, as labeled in Fig. 6a. The cell breadth b is defined as the maximum continuous length of the unit cell along the tensile direction, which is always tangential to the inner edge of the crest. The rationale of choosing the three new geometric variables are offered as follows. First, we postulate that when the substrate is stiff enough to suppress any in-plane rotation or out-of-plane twist, the effect of substrate constraint on serpentines along the tensile direction is very similar to that of substrate-bonded stiff island (Yang and Lu 2013), whose 2D plane strain model is pictured in Fig. 6b, where the island length is equivalent to the serpentine cell breadth b. Hence the "island-to-substrate" length ratio is captured by b/s. However, serpentine is more complex than rectangular islands in the sense that there will be stress/strain concentration at the inner edge of the crest. To capture the effect of arc curvature we choose the dimensionless variable b/r. Also, our previous plane strain serpentine study (Widlund et al. 2014) made us aware that uniaxial tension will introduce significant bending moment at the inner edge of the crest and the bending induced strain is sensitive to the dimensionless variable w/h. Finally, the three new variables of our choice, b/s, b/r, and w/h, can be expressed in terms of the three basic independent dimensionless variables w/r, l/r and α as follows:

$$\frac{w}{h}=\frac{\frac{w}{r}}{2+\frac{w}{r}+\frac{l}{r}\cos(\alpha)+2\sin(\alpha)} \tag{5}$$

where

$$\begin{aligned}\alpha_0&=-\arcsin\left(\left(2-\frac{w}{r}\right)\Big/\left(2+\frac{w}{r}\right)\right)\\ l_0&=-\sec(\alpha)\left(2-\frac{w}{r}+\left(2+\frac{w}{r}\right)\sin(\alpha)\right)\frac{r}{2}\\ l_1&=\sec(\alpha)\left(-2+\frac{w}{r}-2\sin(\alpha)\right)r\\ k&=-\left(\frac{l}{r}\cos(\alpha)+2\sin(\alpha)\right)\\ &\quad\times\left(2-\frac{w}{r}+\frac{l}{r}\cos(\alpha)+2\sin(\alpha)\right)\end{aligned} \tag{6}$$

For every serpentine shape, we are able to convert the three independent geometrical variables, w/r, l/r, and α, to b/s, b/r, and w/h using Eqs. (3)–(5). We also define a dimensionless parameter, λ, which is a function of b/s, b/r, and w/h and is assumed to be linearly related to $\varepsilon_{\max}/\varepsilon_{\text{app}}$ through

$$\frac{\varepsilon_{\max}}{\varepsilon_{\text{app}}}=P_1\lambda+P_2 \tag{7}$$

Equation (7) suggests that the stretchability of the serpentine is completely determined by λ. To obtain P_1 and P_2, we build FEMs for different serpentine shapes, i.e. different combinations of b/s, b/r, and w/h, and find the following best tested empirical equation for λ which offers the highest coefficient of determination ($R^2=0.9873$) for the linear regression in Eq. (7):

$$\lambda=\left(\frac{b}{s}\right)^{0.15}\times\left(\frac{b}{r}\right)^{0.38}\times\left[\left(\frac{w}{h}\right)^2-0.32\frac{w}{h}+0.42\right] \tag{8}$$

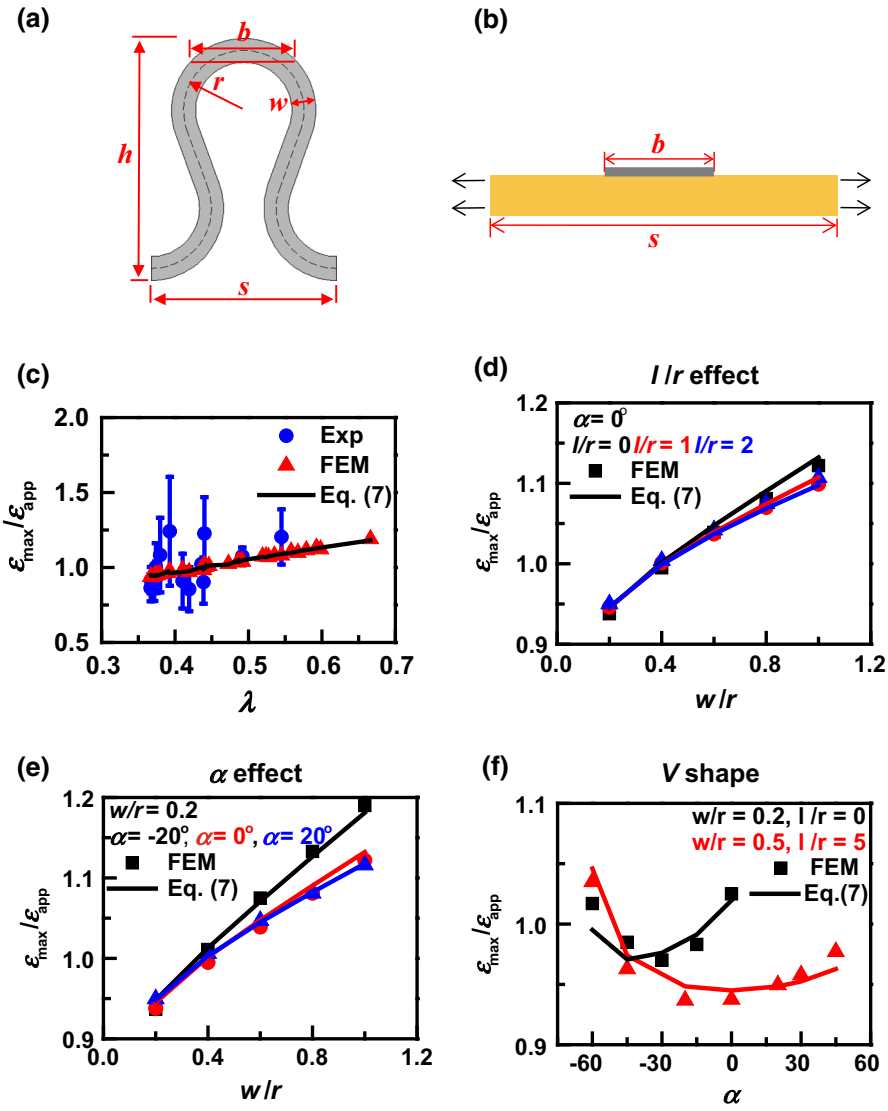

Fig. 6 Empirical relation between maximum strain and geometry. **a** Three new geometric variables that can be grouped in to one dimensionless parameter λ. **b** A 2D schematic of island-on-polymer structure under uniaxial tension. **c** A linear empirical relation between strain and λ is validated by FEM and experiments. Plots of FEM and Eq. (7) for **d** maximum strain versus w/r relation with different l/r, **e** maximum strain versus w/r relation with different α, and **f** maximum strain versus α relation with different w/r and l/r

The corresponding linear regression coefficients are hence obtained as $P_1 = 0.0082$, and $P_2 = 0.0064$.

Comparison between experiments, FEM, and Eq. (7) is given by Fig. 6c. All FEM results are able to fall on the linear curve represented by Eq. (7) attributing to the high R^2 value achieved with the λ given by Eq. (8). The experimental data also demonstrates reasonable agreement with limited scatter. This plot is a direct validation of our empirical relation between maximum strain and geometry as given by Eqs. (7) and (8). Figure 6d, e is plotting $\varepsilon_{max}/\varepsilon_{app}$ as a function of w/r for different l/r and α, respectively, using both the FEM results and Eq. (7). As expected, Eq. (7) captures the FEM results very well and w/r always has a monotonic effect on $\varepsilon_{max}/\varepsilon_{app}$, similar to the conclusion drawn by Fig. 5c. This monotonic dependence can be understood as follows. Since λ increases monotonically with b/r according to Eq. (8) and b/r increases monotonically with w/r according to Eq. (4), the monotonic relation between $\varepsilon_{max}/\varepsilon_{app}$ and λ in Eq. (7) indicates a monotonic relation between $\varepsilon_{max}/\varepsilon_{app}$ and w/r. Another important finding is that when w/r is beyond about 0.4, $\varepsilon_{max}/\varepsilon_{app}$ will be beyond 1, which means the stretchability of the serpentine will actually be lower than their straight counterpart, indicating a strain concentration instead of strain reduction effect. Compared to the effect of w/r, the effects of arm length l/r (Fig. 6c) and arc angle α (Fig. 6d) are

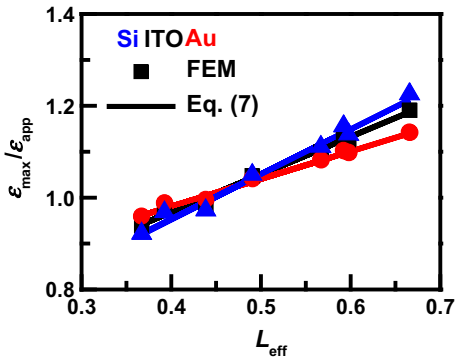

Fig. 7 The linear relation between maximum strain and λ as given by Eq. (8) holds for other serpentine materials such as gold and silicon bonded to stiff polymer substrates such as Kapton or PET with different linear regression coefficients as given in Table 1

not as significant, especially when w/r is small, which is qualitatively consistent with our experimental observation given by Fig. 5d, e. Figure 6f demonstrates the nonmonotonic effect of α on the strains in horseshoe–shaped [Group (c) of Fig. 2b] and V-shaped [Group (d) of Fig. 2(b)] serpentines. Minimum strains in both types of serpentines occur at some intermediate α values. As α deviates from the optimum point, the strains in the serpentines will increase in both directions. Again Eq. (7) can successfully capture this nonmonotonic dependence attributing to the inclusion of a second order polynomial of w/h in Eq. (8).

To prove that Eq. (8) is generic for other serpentine film-stiff polymer substrate pairs, we perform FEM on systems like gold serpentine on Kapton substrate and silicon serpentine on Kapton substrate. The following Young's moduli are adopted: $E_{\mathrm{ITO}} = 118$ GPa, $E_{\mathrm{Au}} = 79$ GPa, $E_{\mathrm{Si}} = 150$ GPa, and $E_{\mathrm{K}} = 2.5$ GPa, respectively. Figure 7 shows the FEM and fitted Eq. (7) with different P_1 and P_2 coefficients as listed in Table 1 using the same Eq. (8). Therefore the λ given by Eq. (8) is verified to be applicable to different film-substrate material combinations as long as the substrate is stiff enough to suppress any in-plane rotation or out-of-plane twist of the serpentine. Another popular stiff polymer substrate widely used in flexible electronics is polyethylene terephthalate (PET) whose modulus is the same as Kapton, which means the P coefficients listed in Table 1 are also applicable for serpentines bonded to PET substrates.

Table 1 P_1 and P_2 for ITO, gold and silicon serpentines on Kapton substrate

	ITO	Gold	Silicon
P_1	0.0082	0.0060	0.0098
P_2	0.0064	0.0074	0.0056

All of our available FEM and experimental results have testified that our empirical equation (Eq. 7) is highly effective in predicting the stretchability of brittle serpentine thin films supported by stiff polymer substrates. Hence the ultimate recommendation of enhancing the stretchability of stiff-polymer supported serpentines is to minimize their λ as given by Eq. (8). Since b/s, b/r and w/h are coupled variables such that varying anyone of them will change the others, there is no simple solution to minimize the effective length by simply tuning the independent variables w/r, l/r, and α. Therefore we list all the shapes we have modeled in Fig. 8 in the order of increased $\varepsilon_{\max}/\varepsilon_{\mathrm{app}}$, i.e. decreased stretchability. The most straightforward conclusion is that serpentines with smaller w/r always exhibits lower strain or higher stretchability. It is worth pointing out that when bonded to stiff polymer substrates, significantly varied serpentine geometries are only able to tune the normalized maximum strain between 0.945 and 1.181 %, a much narrower range compared to free-standing or less constrained serpentines.

5 Conclusions

Effects of serpentine width, arm length, arc radius, and arc angle on the stretchability of Kapton-supported serpentine ITO thin films have been characterized experimentally and modeled by FEM. The strong constraint from the stiff Kapton substrate almost completely prevents the serpentines from in-plane rotation or out-of-plane twist, which leads to very limited effects of the serpentine geometry. Compared to straight ITO-on-Kapton specimens, ITO serpentines with small width-to-radius ratios demonstrate higher stretchability. When the width-to-radius ratio gets beyond 0.4, the stretchability of serpentine ribbons can be even lower than linear ribbons. Although the arm length has almost no effect on serpentine stretchability, the arc angle have some nonmonotonic effects. These experimental and FEM findings have been well explained by a generic

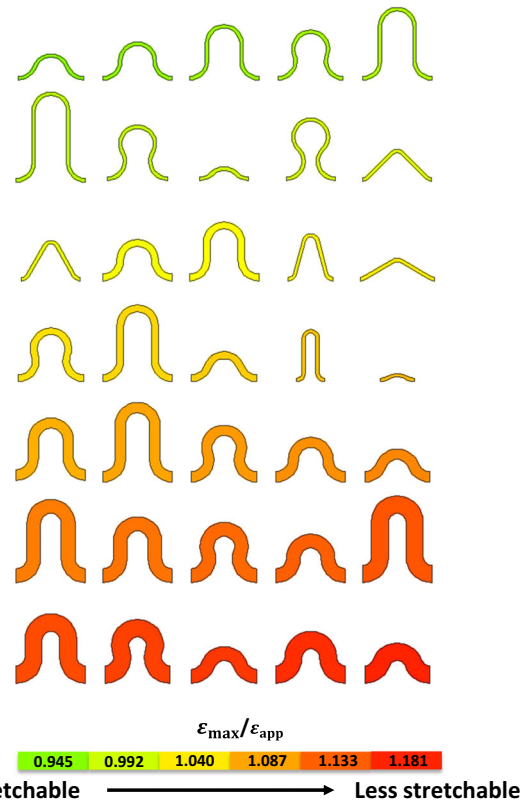

Fig. 8 Serpentine shapes displayed in the order of increased maximum strain, i.e. decreased stretchability. The maximum strains in different serpentine shapes only differ slightly due to the constraint of the stiff substrate

hypothesis that the maximum strain in the serpentine thin film is linearly related to a dimensionless parameter, whose empirical form has been determined by fitting FEM results. Our empirical equation is proved to be applicable to serpentine ribbons of other stiff materials bonded to stiff polymer substrates. Note that the conclusions reached in this paper are not applicable to serpentine ribbons bonded to soft polymer substrates which somewhat allow in-plane arm rotation as well as out-of-plane bending and twisting.

Acknowledgments This work is supported by the NASCENT (Nanomanufacturing Systems for Mobile Computing and Mobile Energy Technologies) Center under NSF Grant No. 1160494. The authors thank Prof. Brian Korgel and Mr. Taylor Harvey for the use of their sputter system to deposit some early batches of the ITO samples. S.Y. acknowledges the George J. Heuer, Jr. Ph.D. endowed graduate fellowship.

References

Betz U, Olsson MK, Marthy J, Escola MF, Atamny F (2006) Thin films engineering of indium tin oxide: large area flat panel displays application. Surf Coat Technol 200:5751–5759. doi:10.1016/j.surfcoat.2005.08.144

Gray DS, Tien J, Chen CS (2004) High-conductivity elastomeric electronics. Adv Mater 16:393–397. doi:10.1002/adma.200306107

Hsu YY, Gonzalez M, Bossuyt F, Axisa F, Vanfleteren J, De Wolf I (2009) In situ observations on deformation behavior and stretching-induced failure of fine pitch stretchable interconnect. J Mater Res 24:3573–3582. doi:10.1557/Jmr.2009.0447

Hsu YY, Gonzalez M, Bossuyt F, Vanfleteren J, De Wolf I (2011) Polyimide-enhanced stretchable interconnects: design fabrication, and characterization. IEEE Trans Electron Dev 58:2680–2688. doi:10.1109/Ted.2011.2147789

Huang X, Yeo WH, Liu YH, Rogers JA (2012) Epidermal differential impedance sensor for conformal skin hydration monitoring. Biointerphases 7:1–9. doi:10.1007/S13758-012-0052-8

Khang DY, Jiang HQ, Huang Y, Rogers JA (2006) A stretchable form of single-crystal silicon for high-performance electronics on rubber substrates. Science 311:208–212. doi:10.1126/science.1121401

Kim DH et al (2008) Materials and noncoplanar mesh designs for integrated circuits with linear elastic responses to extreme mechanical deformations. Proc Natl Acad Sci USA 105:18675–18680. doi:10.1073/pnas.0807476105

Kim DH, Ghaffari R, Lu NS, Rogers JA (2012) Flexible and stretchable electronics for bio-integrated devices. Ann Rev Biomed Eng 14:113–128

Kim DH et al (2011a) Materials for multifunctional balloon catheters with capabilities in cardiac electrophysiological mapping and ablation therapy. Nat Mater 10:316–323. doi:10.1038/Nmat2971

Kim DH et al (2011b) Epidermal electronics. Science 333:838–843. doi:10.1126/science.1206157

Kim RH et al (2011c) Stretchable, transparent graphene interconnects for arrays of microscale inorganic light emitting diodes on rubber substrates. Nano Lett 11:3881–3886. doi:10.1021/Nl202000u

Leterrier Y et al (2004) Mechanical integrity of transparent conductive oxide films for flexible polymer-based displays. Thin Solid Films 460:156–166. doi:10.1016/j.tsf.2004.01.052

Li T, Suo ZG, Lacour SP, Wagner S (2005) Compliant thin film patterns of stiff materials as platforms for stretchable electronics. J Mater Res 20:3274–3277. doi:10.1557/Jmr.2005.0422

Lu NS, Wang X, Suo Z, Vlassak J (2007) Metal films on polymer substrates stretched beyond 50%. Appl Phys Lett 91:221909. doi:10.1063/1.2817234

Lu NS, Suo ZG, Vlassak JJ (2010) The effect of film thickness on the failure strain of polymer-supported metal films. Acta Mater 58:1679–1687. doi:10.1016/j.actamat.2009.11.010

Niu RM, Liu G, Wang C, Zhang G, Ding XD, Sun J (2007) Thickness dependent critical strain in submicron Cu films

adherent to polymer substrate. Appl Phys Lett 90. doi:10.1063/1.2722684

Peng C, Jia Z, Bianculli D, Li T, Lou J (2011) In situ electromechanical experiments and mechanics modeling of tensile cracking in indium tin oxide thin films on polyimide substrates. J Appl Phys 109:1035. doi:10.1063/1.3592341

Peng C, Jia Z, Henry N, Teng L, Jun L (2012) In situ electromechanical experiments and mechanics modeling of fracture in indium tin oxide-based multilayer electrodes. Adv Eng Mater 15. doi:10.1002/adem.201200169

Rogers JA et al (2001) Paper-like electronic displays: large-area rubber-stamped plastic sheets of electronics and microencapsulated electrophoretic inks. Proc Natl Acad Sci USA 98:4835–4840. doi:10.1073/pnas.091588098

Schmidt H, Flugge H, Winkler T, Bulow T, Riedl T, Kowalsky W (2009) Efficient semitransparent inverted organic solar cells with indium tin oxide top electrode. Appl Phys Lett 94. doi:10.1063/1.3154556

Sekitani T, Someya T (2012) Stretchable organic integrated circuits for large-area electronic skin surfaces. MRS Bull 37:236–245. doi:10.1557/Mrs.2012.42

Service RF (2006) Materials science—inorganic electronics begin to flex their muscle. Science 312:1593–1594. doi:10.1126/science.312.5780.1593

Sun YG, Choi WM, Jiang HQ, Huang YGY, Rogers JA (2006) Controlled buckling of semiconductor nanoribbons for stretchable electronics. Nat Nanotechnol 1:201–207. doi:10.1038/nnano.2006.131

Webb RC et al (2013) Ultrathin conformal devices for precise and continuous thermal characterization of human skin. Nat Mater 12:938–944. doi:10.1038/nmat3755. http://www.nature.com/nmat/journal/v12/n10/abs/nmat3755.html#supplementary-information

Widlund T, Yang S, Hsu Y-Y, Lu N (2014) Stretchability and compliance of freestanding serpentine-shaped ribbons. Int J Solids Struct 51:4026–4037. doi:10.1016/j.ijsolstr.2014.07.025

Xu S et al (2013) Stretchable batteries with self-similar serpentine interconnects and integrated wireless recharging systems. Nat Commun 4. doi:10.1038/Ncomms2553

Yang S, Lu N (2013) Gauge factor and stretchability of silicon-on-polymer strain gauges. Sensors 13:8577–8594

Yeo W-H et al (2013) Multi-functional electronics: multifunctional epidermal electronics printed directly onto the skin (Adv. Mater. 20/2013). Adv Mater 25:2772–2772. doi:10.1002/adma.201370133

Yoon J et al (2008) Ultrathin silicon solar microcells for semitransparent, mechanically flexible and microconcentrator module designs. Nat Mater 7:907–915. doi:10.1038/Nmat2287

Zhang Y et al (2013) Mechanics of ultra-stretchable self-similar serpentine interconnects. Acta Mater 61:7816–7827. doi:10.1016/j.actamat.2013.09.020

Zhang YH et al (2013b) Buckling in serpentine microstructures and applications in elastomer-supported ultra-stretchable electronics with high areal coverage. Soft Matter 9:8062–8070. doi:10.1039/C3sm51360b

Zhang YH et al (2014) A hierarchical computational model for stretchable interconnects with fractal-inspired designs. J Mech Phys Solids 72:115–130. doi:10.1016/j.jmps.2014.07.011

Zheng J, Peng C, Jun L, Teng L (2012) A map of competing buckling-driven failure modes of substrate-supported thin brittle films. Thin Solid Films 520. doi:10.1016/j.tsf.2012.07.011